#### **OPEN ACCESS**



# The Observable Properties of Galaxy Accretion Events in Milky Way–like Galaxies in the FIRE-2 Cosmological Simulations

Danny Horta<sup>1,2</sup>, Emily C. Cunningham<sup>1,3,10</sup>, Robyn E. Sanderson<sup>1,4</sup>, Kathryn V. Johnston<sup>1,3</sup>, Nondh Panithanpaisal<sup>4</sup>, Arpit Arora<sup>4</sup>, Lina Necib<sup>5,6</sup>, Andrew Wetzel<sup>7</sup>, Jeremy Bailin<sup>8</sup>, and Claude-André Faucher-Giguère<sup>9</sup>, Center for Computational Astrophysics, Flatiron Institute, 162 5th Ave., New York, NY 10010, USA; dhortadarrington@flatironinstitute.org

2 Astrophysics Research Institute, Brownlow Hill, Liverpool, L3 5RF, UK

3 Department of Astronomy, Columbia University, 550 West 120th Street, New York, NY 10027, USA

4 Department of Physics & Astronomy, University of Pennsylvania, 209 S 33rd St., Philadelphia, PA 19104, USA

5 The NSF AI Institute for Artificial Intelligence and Fundamental Interactions, USA

6 Department of Physics and Kavli Institute for Astrophysics and Space Research, Massachusetts Institute of Technology, 77 Massachusetts Ave, Cambridge MA

02139, USA

Department of Physics and Astronomy, University of California, Davis, CA 95616, USA
 Department of Physics and Astronomy, University of Alabama, Tuscaloosa, AL 35487, USA
 Department of Physics and Astronomy and CIERA, Northwestern University, 1800 Sherman Avenue, Evanston, IL 60201, USA
 Received 2022 November 8; revised 2022 December 15; accepted 2022 December 21; published 2023 February 6

#### **Abstract**

In the  $\Lambda$ -Cold Dark Matter model of the universe, galaxies form in part through accreting satellite systems. Previous works have built an understanding of the signatures of these processes contained within galactic stellar halos. This work revisits that picture using seven Milky Way-like galaxies in the Latte suite of FIRE-2 cosmological simulations. The resolution of these simulations allows a comparison of contributions from satellites above  $M_* \gtrsim 10 \times 7 M_{\odot}$ , enabling the analysis of observable properties for disrupted satellites in a fully self-consistent and cosmological context. Our results show that the time of accretion and the stellar mass of an accreted satellite are fundamental parameters that in partnership dictate the resulting spatial distribution, orbital energy, and  $[\alpha/\text{Fe}]$ -[Fe/H] compositions of the stellar debris of such mergers at present day. These parameters also govern the resulting dynamical state of an accreted galaxy at z=0, leading to the expectation that the inner regions of the stellar halo ( $R_{GC} \lesssim 30 \, \text{kpc}$ ) should contain fully phase-mixed debris from both lower- and higher-mass satellites. In addition, we find that a significant fraction of the lower-mass satellites accreted at early times deposit debris in the outer halo ( $R_{GC} > 50 \, \text{kpc}$ ) that are not fully phased-mixed, indicating that they could be identified in kinematic surveys. Our results suggest that, as future surveys become increasingly able to map the outer halo of our Galaxy, they may reveal the remnants of long-dead dwarf galaxies whose counterparts are too faint to be seen in situ in higher-redshift surveys.

Unified Astronomy Thesaurus concepts: Galaxy formation (595); Milky Way Galaxy (1054); Milky Way stellar halo (1060); Milky Way dynamics (1051)

#### 1. Introduction

A fundamental prediction from the current cosmological paradigm (Λ-CDM) is that galaxies grow in great measure via the process of hierarchical mass assembly (Searle & Zinn 1978; Bullock & Johnston 2005). As a result, stellar halos of galaxies are expected to host large quantities of accreted material in the form of phase-mixed debris, streams, and satellite galaxies (e.g., Johnston et al. 1996; Helmi et al. 1999; Bullock & Johnston 2005; Johnston et al. 2008; Cooper et al. 2010; Font et al. 2011). This accreted component is unique for each galaxy and is dictated by its accretion history (e.g., Bullock & Johnston 2005; De Lucia & Helmi 2008; Johnston et al. 2008; Gómez et al. 2012; Tissera et al. 2012).

Halo substructures believed to be the remains of cannibalized systems have been discovered in the Milky Way (MW; e.g., Ibata et al. 1994; Helmi et al. 1999; Belokurov et al. 2018; Haywood et al. 2018; Helmi et al. 2018; Koppelman et al. 2019;

Original content from this work may be used under the terms of the Creative Commons Attribution 4.0 licence. Any further distribution of this work must maintain attribution to the author(s) and the title of the work, journal citation and DOI.

Mackereth et al. 2019; Myeong et al. 2019; Naidu et al. 2020; Yuan et al. 2020; Horta et al. 2021a), Andromeda (e.g., Ibata et al.2007; McConnachie et al. 2009; Veljanoski et al. 2014), and nearby galaxies (e.g., Martínez-Delgado et al. 2008; Atkinson et al. 2013; Duc et al. 2015; Crnojević et al. 2016; Chiti et al. 2021). The characterization of such debris in observable spaces such as kinematics, chemistry, and age provide an opportunity to study the remains of the many galaxies destroyed by the MW that did not survive to z=0 on a star-by-star basis, and enable the opportunity to develop a deeper understanding on how these building blocks contribute to the formation and evolution of the Galaxy.

We are now in the era of large-scale stellar surveys of the MW. The data collected from the revolutionary Gaia mission (Gaia Collaboration et al. 2018, 2021), as well as the latest wide-field spectroscopic programs such as APOGEE (Majewski et al. 2017), GALAH (De Silva et al. 2015), RAVE (Steinmetz et al. 2020), LAMOST (Cui et al. 2012), and H3 (Conroy et al. 2019), among others, are providing a colossal archive of chemo-dynamical properties for millions of stars in the MW. This is paving the way for new discoveries of substructure in the stellar halo component of the Galaxy (and halos of other Local Group galaxies), as well as tighter constraints on the density profile and shape (e.g., Deason et al. 2011; Iorio et al. 2018; Deason et al. 2019;

<sup>&</sup>lt;sup>10</sup> NASA Hubble Fellow.

Iorio & Belokurov 2019; Deason et al. 2021), the mass of its different stellar populations (e.g., Mackereth & Bovy 2020; Horta et al. 2021b; Deason et al. 2021; Limberg et al. 2022), its chemical properties (e.g., Schiavon et al. 2017; Hayes et al. 2018; Mackereth et al. 2019; Matsuno et al. 2019; Monty et al. 2020; Buder et al. 2022; Kisku et al. 2021; Limberg et al. 2021; Horta et al. 2022), and the perturbations to its stellar/dark matter components from its interaction with its massive satellites (e.g., Cunningham et al. 2020; Erkal et al. 2021; Garavito-Camargo et al. 2021; Conroy et al. 2021; Vasiliev et al. 2021). However, although the great strides performed on the observational front are shedding light on the nature and accretion history of our Galaxy, there is still a demand to interpret such observational findings theoretically in a cosmological setting using high-resolution simulations.

Since the classic papers by Bullock & Johnston (2005) and Johnston et al. (2008), many works have sought to interpret the resulting phase-space and orbital distribution of stars in the stellar halos of galaxies from a theoretical standpoint (e.g., Cooper et al. 2010; Pillepich et al. 2014; Amorisco 2017a), and specifically for MW-like galaxies (e.g., Font et al. 2011; McCarthy et al. 2012; Deason et al. 2013, 2015, 2016; Amorisco 2017b; D'Souza & Bell 2018; Monachesi et al. 2019; Evans et al. 2020; Fattahi et al. 2020; Font et al. 2020; Grand et al. 2020; Santistevan et al. 2020; Grand et al. 2021; Nikakhtar et al. 2021; Panithanpaisal et al. 2021; Cunningham et al. 2022). The results from such efforts have helped reveal the diversity and complexity of substructure in the stellar halos of galaxies like our own MW, and have helped shed light on the properties of discovered debris in the stellar halo of the Galaxy resulting from hierarchical mass assembly. However, many of these results were either used in: (i) the regime of tailored/idealized N-body simulations; (ii) the context of large cosmological simulations that do not match the high-resolution needed to study the intricacies of this hierarchical formation process.

In this work, we set to test if expectations from tailored *N*-body simulations survive when examining the observable properties of the debris from disrupted satellite galaxies using high-resolution (zoom-in) cosmological simulations. We ask three main questions:

- 1. "What are the properties of disrupted satellites?"
- 2. "Do our expectations from prior simulations survive in a high-resolution and cosmological setting?"
- 3. "What do these results mean for future surveys?"

We make use of the sophisticated Feedback In Realistic Environments (i.e., FIRE-2; Hopkins et al. 2018a) suite of numerical cosmological simulations to explore the distributions of halo star properties in spatial, orbital, and chemical planes as a function of their progenitor stellar mass and infall time. Our aim is to understand the relationship between merger mass and infall time with the distribution of the resulting stellar particles of independent merger events in diagnostic planes that can be compared with observational findings. Moreover, we also aim to obtain results that can be used as a theoretical blueprint for upcoming surveys, such as WEAVE (Dalton et al. 2014), 4MOST (de Jong et al. 2019), DESI (Allende Prieto et al. 2020), MWM/SDSS-V (Kollmeier et al. 2017), or the Rubin Observatory's LSST (Ivezić et al. 2019), which will likely pave the way for new discoveries of debris from accreted satellites

lurking in the outer regions of the Galactic stellar halo, and the characterization of the ones already known.

This paper is structured as follows: in Section 2, we describe the simulations used in this work and the methodology employed to identify accretion events in the Latte/FIRE-2 cosmological simulations. Subsequently, we present the results obtained in this work, where we show how different mass/infall time accretion events deposit the bulk of their stars as a function of their spatial coordinates in Section 3, their orbital parameters in Section 4, and their chemical compositions in Section 5. We then discuss the implications of our results and present our concluding statements in Section 6.

# 2. Simulations and Satellite Sample

## 2.1. Simulations

We make use of seven MW-like galaxies from the Latte suite of FIRE-2<sup>11</sup> cosmological zoom-in simulations (Wetzel et al. 2016). These simulations were run with the FIRE-2 physics model (Hopkins et al. 2018a), utilizing the Lagrangian meshless finite-mass N-body gravitational plus hydrodynamics code GIZMO<sup>12</sup> (Hopkins 2015). FIRE-2 simulations model several radiative cooling and heating processes for gas such as free-free emission, photoionization/recombination, Compton scattering, photoelectric, metal-line, molecular, fine-structure, dust-collisional, and cosmic-ray heating across a temperature range of 10-10<sup>10</sup> K. These simulations also include the spatially redshift-dependent and spatially uniform cosmic UV background from Faucher-Giguère et al. (2009), for which H I reionization occurs at  $z_{\rm reion} \sim 10$ . Moreover, FIRE-2 selfconsistently generates and tracks 11 chemical abundance species (namely, H, He, C, N, O, Ne, Mg, Si, S, Ca, and Fe), including subgrid diffusion of these abundances in gas via turbulence (Hopkins 2016; Su et al. 2017; Escala et al. 2018), as well as enrichment from stellar winds.

The simulations in this work all use a starting mass resolution of 7100  $M_{\odot}$  for gas particles and a fixed resolution of 35,000  $M_{\odot}$  for dark matter particles. Star formation occurs in gas that is self-gravitating, Jeans-unstable, cold  $(T < 10^4 \text{K})$ , dense ( $n > 1000 \text{ cm}^{-3}$ ), and molecular (following Krumholz & Gnedin 2011). As each star particle forms, it inherits the mass and chemical abundance composition of its progenitor gas particle and represents a single stellar population with a Kroupa (2001) initial mass function. This population evolves according to the STARBURST v7.0 models (Leitherer et al. 1999), so the star particle decreases in mass with time as the most massive stars die. By the present day, most star particles have a mass of 4000–5000  $M_{\odot}$ . Stellar evolution gives rise to localized feedback at the location of each star particle, including corecollapse and Ia supernovae, mass loss from stellar winds, and radiation, including radiation pressure, photoionization, and photoelectric heating. Implementation of these processes follows the descriptions in Hopkins et al. (2018a) and Hopkins et al. (2018b).

The Latte suite was generated within periodic cosmological boxes of lengths 70.4–172 Mpc using the code MUSIC (Hahn & Abel 2011), and constructing cosmological zoom-in initial conditions for each simulation at  $z \simeq 99$ . Each simulation has 600 snapshots saved down to z = 0, spaced every  $\simeq 25$  Myr. All

<sup>11</sup> FIRE project website: http://fire.northwestern.edu.

<sup>12</sup> http://www.tapir.caltech.edu/~phopkins/Site/GIZMO.html

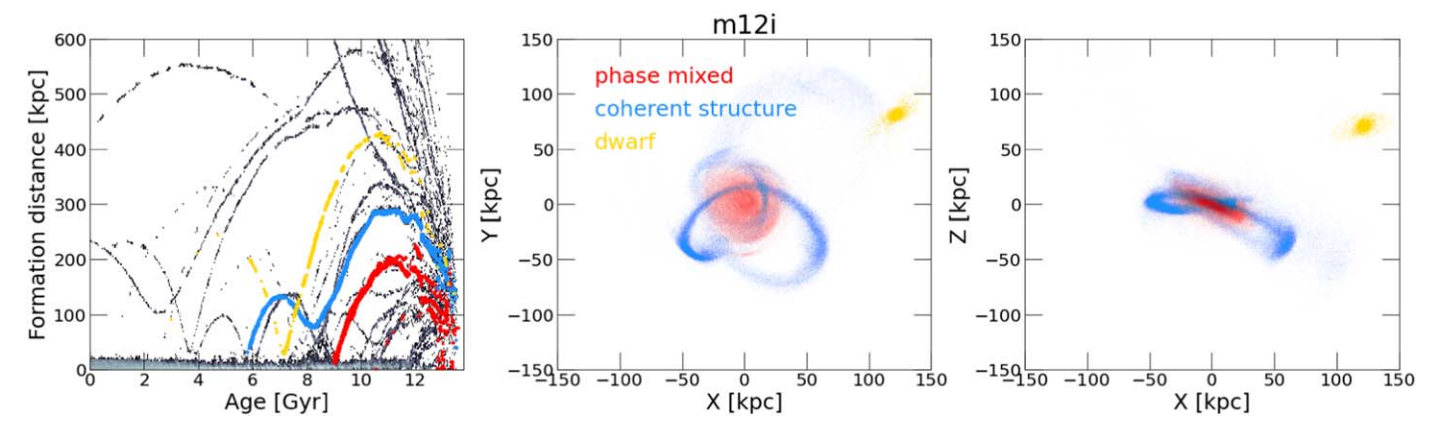


Figure 1. Left: Density distribution showing the formation distance as a function of age for all the star particles in the Latte halo m12i. Here, every "branch"-like feature corresponds to a different subhalo, some of which subsequently merge with the main host (MW-like) halo with time (see Cunningham et al. (2022) for an introduction to this diagnostic plane). Highlighted as red/blue/yellow branches are three accretion events identified for this simulation, corresponding to phase-mixed/coherent-stream/dwarf classified accretion events, respectively. Middle: face-on projection of the star particles associated with the illustrated accretion events centered on the m12i MW-like Galaxy. Right: star particles associated with the illustrated accretion events, again centered on the m12i MW-like Galaxy, but now from an edge-on projection.

simulations assume flat  $\Lambda\text{-CDM}$  cosmology with parameters consistent with Planck Collaboration et al. (2020). More specifically, the Latte suite (excluding m12r and m12w) used  $\Omega_{\rm m}=0.272,\,\Omega_{\rm b}=0.0455,\,\sigma_8=0.807,\,n_{\rm s}=0.961,\,h=0.702.$  The m12r and m12w halos were selected specifically because they host an LMC-mass satellite galaxy, and adopted updated initial conditions from (Planck Collaboration et al. 2020) compared to their MW-mass galaxy siblings:  $h=0.68,\,\Omega_{\Lambda}=0.31,\,\Omega_{\rm m}=0.31,\,\Omega_{\rm b}=0.048,\,\sigma_8=0.82,\,n_{\rm s}=0.961,\,$  and h=0.97.

The resolution of this suite of simulations enables baryonic subhalos to be well-resolved even near each MW-like galaxy. It also resolves the formation of tidal streams from satellite galaxies down to approximately  $10^8 M_{\odot}$  in total mass or  $10^6 M_{\odot}$  in stellar mass (at z = 0), similar to that of the MW's "classical" dwarf spheroidals (e.g., Panithanpaisal et al. 2021; Cunningham et al. 2022; Shipp et al. 2022). Furthermore, dark matter particles in each snapshot are processed with Rockstar (Behroozi et al. 2013a) to produce halo catalogs that are connected in time using consistent trees to form a merger tree (Behroozi et al. 2013b). Once a merger tree is constructed, a preliminary assignment of star particles to each halo and subhalo, identified by Rockstar in each snapshot, is made by selecting star particles within the halo's virial radius and within twice the halo circular velocity relative to the halo's center. Thus, all galaxies are tracked within the simulated volume across all snapshots. The post-processing is done using gizmo analysis (Wetzel & Garrison-Kimmel 2020a) and halo analysis (Wetzel & Garrison-Kimmel 2020b).

The properties of the host galaxies in Latte show broad agreement with the MW, including the stellar-to-halo mass relation (Hopkins et al. 2018a), stellar halos (Bonaca et al. 2017; Sanderson et al. 2018), and the radial and vertical structure of their disks (Ma et al. 2017; Bellardini et al. 2021). Moreover, the satellite populations of these suite of simulations have also been demonstrated to agree with several observed properties, such as the mass and velocity dispersions (Wetzel et al. 2016; Garrison-Kimmel et al. 2019a), star formation histories (Garrison-Kimmel et al. 2019b), and radial distributions (Samuel et al. 2020). Despite great similarities in the properties of the satellite galaxies in Latte and those of the observed satellites around the MW, it has been shown that the

former are generally too metal-poor when compared to the latter (Escala et al. 2018; Wheeler et al. 2019; Panithanpaisal et al. 2021). This is likely a consequence of the delay time distributions of SNIa (Gandhi et al. 2022). For this work, we emphasize that we do not require quantitative agreement with simulated and observed abundances. The relations found in this paper between (luminous) subhalo parameters and their respective chemical abundances should be treated qualitatively, and they are intended for use within the simulations only. However, although the *normalization* of the various abundances is not always in good agreement with observations, we expect the *trends* we identify in this paper to be robust.

#### 2.2. Identifying Accretion Events in the Simulations

In this subsection, we describe the method for identifying accretion events in each cosmological simulation. Each accretion event identified in this work was selected based on a set of criteria, building on the selection method from Panithanpaisal et al. (2021).

The first step involves inspecting the density distribution of star particles in each simulation in the age-formation distance plane at z = 0, first introduced in Cunningham et al. (2022) and Khoperskov et al. (2022a), as shown in Figure 1. Here, star particle ages are shown on the x-axis, and the formation distance of star particles (defined as the distance of the star particle at its formation time from the center of the main MWlike host) is on the y-axis. The grayscale color in this panel indicates the density of star particles for the Latte galaxy m12i (first introduced in Wetzel et al. 2016 13). In this plane, many branch structures (i.e., luminous subhalos) appear to merge with the main MW host of the simulation (namely, the highdensity region at formation distance <25 kpc). Star particles that form in the branches at large formation distances are stars forming in dwarf galaxies, some of which enter the main host halo and are disrupted. Thus, we use the branches in this plane to identify satellite galaxies accreted by the main host galaxy.

Once a clear merger event was identified in the ageformation distance plane, the next step involved using the halo catalog for each simulation to identify the luminous subhalo ID

<sup>13</sup> The seven MW-like galaxies in Latte studied in this work are referred to as m12b, m12c, m12f, m12i, m12m, m12r, and m12w.

 Table 1

 Summary of Properties for the Massive Accretion Events Identified in This Work for Every MW-like Halo in the Latte Suite of FIRE-2 Simulations

Simulation	$N_{ m accretions}$	$M_{*, \text{ accretion }} (M_{\odot})$ $(10^7 - 10^8 / 10^8 - 10^9 / > 10^9)$	$\tau_{\text{infall }}(\text{Gyr})$ (<4/4-8/>8)	Classification (Phase-mixed/Coherent-stream/Dwarf)
m12b	9	6–2–1	0-2-7	5–3–1
m12c	6	2–2–2	3-1-2	2–3–1
m12f	11	6–3–2	0-4-7	7–4–0
m12i	12	8-4-0	0-2-10	4–7–1
m12m	14	8-5-1	1-2-11	7–2–4
m12r	4	1–1–2	3-0-1	2–1–1
m12w	7	4–2–1	0-3-4	6-0-1
Total	63	35-19-9	7–14–42	33–20–9
Mean <sup>a</sup>	9	5-2.7-1.3	1-2-6	4.7-2.8-1.3

<sup>&</sup>lt;sup>a</sup> The mean values quoted are only applicable to accretion events studied in this work.

that had the smallest distance to the MW-like host during the time at which the subhalo branch in Figure 1 connected with the host MW-like galaxy branch. By identifying the subhalo ID with the smallest distance, we were able to identify the star particles belonging to the subhalo of interest, using the particle tracking function built within gizmo analysis. We then tracked star particles for that subhalo to z=0 and to the point in which the subhalo first crosses the virial radius of the MW-like host (that is, at the first snapshot in the simulation after the luminous subhalo crosses the virial radius of the host).

The final sample of disrupted satellites used in this work is comprised of 62 accretion events with stellar masses greater than  $M_{\star} > 10^7 \, M_{\odot}$ . We choose to only study disrupted satellites above this mass threshold, as we aim to characterize the observable properties of the debris from the largest (stellar) mass building blocks of the Latte MW-like galaxies. Of this sample of disrupted satellites, 9 belong to m12b, 6 to m12c, 10 to m12f, 12 to m12i, 14 to m12m, 4 to m12r, and 7 to m12w. From our sample, 35 disrupted satellites have a stellar mass smaller than  $M_{\star} < 10^8 \, M_{\odot}$ , 19 have a stellar mass between  $10^8 \, M_{\odot} < M_{\star} < 10^9 \, M_{\odot}$ , and 8 have a stellar mass greater than  $M_{\star} > 10^9 \, M_{\odot}$ . For more details on the properties of these identified disrupted satellites, we refer the reader to Table 1.

As Panithanpaisal et al. (2021) recently studied stream progenitors in the suite of simulated MW-like galaxies we use in this work, it is worth comparing the overlap between the corresponding samples. We use a higher mass cut of  $M_{\star}$  >  $10^7 M_{\odot}$  in this work, rather than the  $M_{\star} = 10^{5.5} M_{\odot}$  used in Panithanpaisal et al. (2021). Moreover, Panithanpaisal et al. (2021) selected stream candidates requiring that they be bound  $\sim$ 2.7–6.5 Gyr ago. Therefore, many of the earlier mergers identified in this work are not included in their catalog. Panithanpaisal et al. (2021) also imposed an upper cutoff on the number of star particles in order to rule out objects that are more massive than the Sagittarius stream, which we did not apply in this work. In summary, we find that 22 of the (massive) accretion events identified by Panithanpaisal et al. (2021) are contained within the initial sample of accretion events identified in this work.

Figure 2 shows the stellar mass of every luminous subhalo at infall time as a function of infall time (defined as the lookback time when the progenitor subhalo first crosses the virial radius of the host MW-like galaxy) for all the mergers identified in this study, color-coded by the virial mass of the progenitor subhalo at infall. The lower panel of Figure 2 shows the time evolution of the virial mass (i.e.,  $M_{\rm DM,host}$ ) for the host MW-like galaxies. Upon determining the final sample of accretion

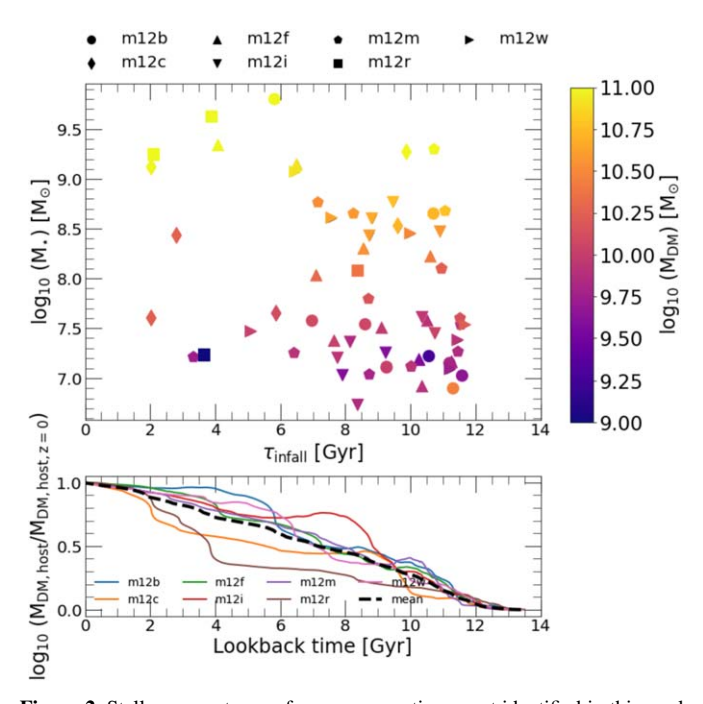


**Figure 2.** Stellar mass at  $\tau_{infall}$  for every accretion event identified in this work as a function of their  $\tau_{infall}$  and color-coded by their virial mass (also at  $\tau_{infall}$ ). The bottom panel shows the growth of each MW-like galaxy as a function of its final virial mass, where we show the mean as a dashed black line.

events in the seven MW-like halos studied, we set out to classify the identified mergers based on how their particles are distributed in phase-space at present day. To do so, we follow the method from Panithanpaisal et al. (2021) (see their Figure 2) and classify the identified mergers into one of the following categories: phase-mixed debris, coherent-stream debris, or bound dwarf/satellite. For a full description of the method used to define the degree of phase mixing (referred to in the rest of this work as dynamical state) of all the identified accretion events, we refer the reader to Section 3.2 in Panithanpaisal et al. (2021). However, we describe the main steps here for clarity and completeness:

Accretion events that have a maximum pairwise separation distance between any two star particles greater than 120 kpc are classified as either coherent streams or phase-mixed candidates. Accretion events that did not satisfy this condition were considered dwarfs/satellites (i.e., accretion events that remain clustered in position space).

Table 2
Useful Definitions

	Merger Classification		
Phase-mixed debris	Accretion event with a maximum pairwise separation distance between any two star particles greater than 120 kpc, whose local velocidispersion of star particles falls above the threshold given by Equation (1)		
Coherent-stream debris	Accretion event with a maximum pairwise separation distance between any two star particles greater than 120 kpc, whose local veloci dispersion of star particles falls below the threshold given by Equation (1)		
Dwarf/satellite	Accretion event with a maximum pairwise separation distance between any two star particles smaller than 120 kpc		
	Parameter definitions		
$ au_{ m infall}$ [Gyr]	Lookback time in the simulation corresponding to the snapshot after which a subhalo crosses the virial radius of the host MW-like Galaxy. For this work, $\tau_{infall}$ is referred to as the time of the accretion event, where the beginning/end of the simulation corresponds to a $\tau_{infall}$ value of 14/0 [Gyr], respectively		
Formation distance [kpc]	Distance of a simulation star particle from the center of the host MW-like galaxy at the time that the star particle was formed		
$M_{\star}$ $[M_{\odot}]$	Stellar mass of the subhalo at $ au_{ m infall}$		
$M_{ m DM} \ [M_{\odot}]$	Virial mass of the subhalo at $ au_{ ext{infall}}$		
$L_{\rm tot} [{\rm kpc} \ {\rm kms}^{-1}]$	Total angular momentum per unit mass of a system at $z = 0$ , defined as $L_{\text{tot}} = \sqrt{L_x^2 + L_y^2 + L_z^2}$ , where $[L_x, L_y, L_z]$ are the three Cartesian		
	coordinates comprising the angular momentum vector L centered on the host MW-like galaxy, and $L = r \times v$ . Here, $r/v$ correspond to the three component Cartesian coordinate position and velocity vector of every star particle with respect to the host MW-like galaxy coordinate system at $z = 0$		
$E [\mathrm{km}^2  \mathrm{s}^{-2}]$	Orbital energy per unit mass of a system at $z=0$ , computed as the average of the orbital energy of all star particles in a system weighted by a particles stellar mass, defined as the sum of the potential and kinetic energies (i.e., $E=\Phi+K$ ). In order to obtain all the MW-like halo energies on the same scale, these are normalized by the orbital energy at $\langle R_{GC} \rangle = 200$ kpc (namely, $E_{200}$ )		
η	Orbital circularity at $z=0$ , defined as $L_{\text{tot}}(E)/L_{\text{circ}}(E)$ . Here, $L_{\text{circ}}$ equates to the angular momentum of a circular orbit with the same orbital energy as each star particle in a system, defined as $L_{\text{circ}} = r_{\text{circ}} \times \nu_{\text{circ}}$ (where $r_{\text{circ}}$ and $\nu_{\text{circ}}$ are the position and velocity vectors, respectively, of a star particle centered on the host MW-like galaxy coordinate system on a circular orbit with the same orbital energy)		

2. Accretion events that have a maximum pairwise separation distance between any two star particles greater than 120 kpc were divided into two further subgroups. Following the method in Panithanpaisal et al. (2021), phase-mixed accretions were distinguished from coherent streams based on an average local velocity dispersion threshold (see Equation (1)). To do so, Panithanpaisal et al. (2021) determine the local velocity dispersion of a star particle using its 7–20 (depending on the size of the system) nearest neighbors in phase space, and then they determine the median over all star particles in the system in order to determine the average local velocity dispersion. This local velocity dispersion threshold is ~20 km s<sup>-1</sup> for a stream candidate with  $M_{\star} \sim 10^7 M_{\odot}$  (see their Figure 1). The analytical expression used by Panithanpaisal et al. (2021) to classify accreted debris can be written as

$$\langle \sigma \rangle = -5.28 \log \left( \frac{M_{\star}}{M_{\odot}} \right) + 53.55,$$
 (1)

in units of km<sup>-1</sup>. Panithanpaisal et al. (2021) determined this relation by using a linear kernel Support Vector Machine (SVM) with disrupted systems in all of the Latte suite of simulations. In practice, coherent streams have lower average local velocity dispersions than phase-mixed debris at fixed  $M_{\star}$ . A summary of the mergers identified and their corresponding properties is listed in Table 1, while a summary of the dynamical state classification and parameter definitions employed in this work is provided in Table 2.

We note that, based on this definition, if two streams of different stellar mass occupy the same physical volume and are on similar orbits, the physical distance between a certain number of star particles (seven in the case of the lower-mass systems in Panithanpaisal+2021) will be more spread out in the less-massive system. Therefore, the local velocity dispersion criterion is higher for the lower-mass systems, to allow for this local resolution effect, even though the total velocity dispersion before disruption is well-resolved. While resolution does impact the local velocity dispersion threshold, which is calculated using 7–20 particles, the quantities plotted and discussed in this work are means and dispersions calculated globally for each progenitor galaxy, using a minimum of 1400 star particles each. Therefore, we do not expect resolution to play a big role for these quantities.

In the following sections, we present the main results obtained in this study: the resulting distributions of massive accretion events in MW-like Galaxies in spatial, orbital, and chemical planes.

# 3. Spatial Distribution

We begin our analysis with an examination of the spatial distribution of the disrupted satellites. This is a property of the accretion events that should be easy to compare to observational findings, and which may serve as an important blueprint for current/upcoming surveys aiming at characterizing the stellar halo of the Milky Way and Andromeda galaxies.

Figure 3 shows the mean Galactocentric radius ( $\langle R_{\rm GC} \rangle$ ) value at z=0 of star particles belonging to every accretion event identified in this work as a function of  $\tau_{\rm infall}$  and color-coded by their stellar mass. The error bars shown in this plot show the average of the difference between the 16th and 84th percentile ranges for the full distribution of each object. The black line defines the mean value for the evolution of the virial radius for the seven Milky Way–like hosts as a function of lookback time.

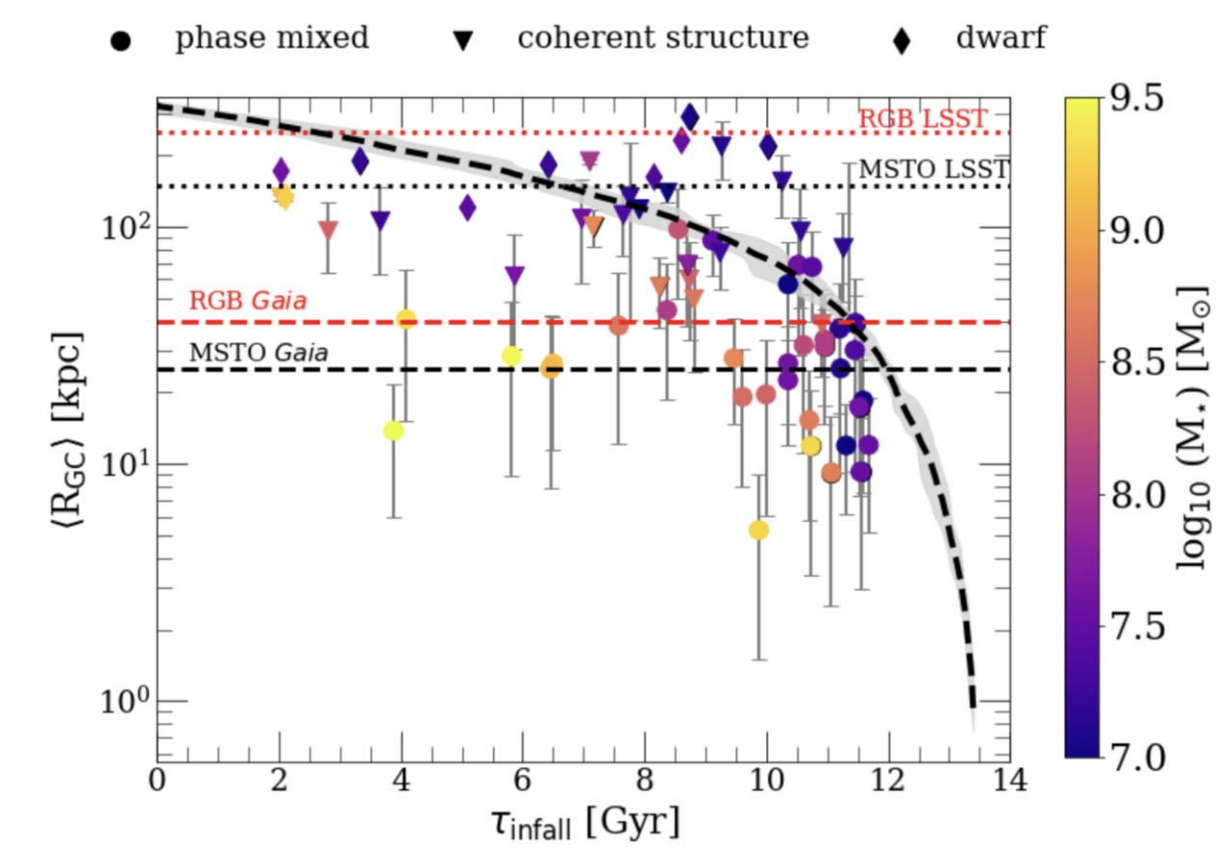


Figure 3. Mean Galactocentric radius value (at z=0) for every accretion event as a function of their merger infall time (where  $\tau_{\rm infall}=0$  corresponds to the present day), color-coded by the stellar mass of each subhalo at the time of infall. The error bars indicate the mean of the 16th and 84th percentile ranges of the star particles. The dashed black line illustrates the mean value of the evolution of the virial radius for the seven Milky Way-like halos used, with the shaded region demarcating the 16th and 84th percentile range. Overplotted are predictions for observing detection limits for individual stars within the Milky Way, from upcoming massive surveys from Sanderson et al. (2019), assuming the faintest ( $r \sim 20.5$ –24.5) limiting magnitudes for RGB and MSTO stars. At large  $\tau_{\rm infall}$ , galaxies of all stellar masses deposit the bulk of their stars close to the galactic center of the host (MW-like) galaxy. However, at fixed  $\tau_{\rm infall}$ , more massive systems tend to deposit the bulk of their stars closer to the host galaxy's center. Furthermore, our results suggest that the smaller-mass systems ( $M_{\star} < 10^8 M_{\odot}$ ) that are accreted at intermediate to low  $\tau_{\rm infall}$  can be contained at large Galactocentric distances, of over 150 kpc, that will only be detectable with upcoming surveys like LSST.

Our results reveal a clear relation between  $\langle R_{\rm GC} \rangle$ , stellar mass, and  $au_{\text{infall}}$ . Here, lower (stellar) mass mergers deposit the bulk of their stars at higher  $\langle R_{GC} \rangle$  than more massive mergers at fixed  $\tau_{infall}$ . We find this to also be the case for total mass (defined in Table 2 as $M_{\rm DM}$ ). For the most massive mergers  $(M_{\star} > 10^8 M_{\odot})$ , the floor  $\langle R_{\rm GC} \rangle$  value increases with decreasing  $au_{\text{infall}}$  as the host MW-like halo grows, rising from a value of  $\langle R_{\rm GC} \rangle < 10$  kpc at  $\tau_{\rm infall} > 10$  Gyr to a value of  $\langle R_{\rm GC} \rangle > 30$  kpc at  $\tau_{\text{infall}}$  < 4 Gyr. Along similar lines, we find that accretion events that deposit the bulk of their stars at higher Galactocentric values ( $\langle R_{GC} \rangle > 40$  kpc) are predominantly low-mass  $(M_{\star} < 10^{7.5} M_{\odot})$ , unless they get accreted closer to z = 0 (i.e., low  $\tau_{\text{infall}}$ ), and are all either coherent streams or bound dwarfs mergers. These accretion events have long dynamical times, allowing the debris from these mergers to remain kinematically coherent in phase space. Conversely, mergers that deposit the bulk of their stars closer to the Galactic center of the MW-like host are predominantly phase-mixed.

It is particularly interesting to ask where we might find the remnants of low-mass, long-dead satellites that would be below the detection limits of higher=redshift studies. At high infall times (namely,  $\tau_{\rm infall} > 11$  Gyr), we find a large number of lower-mass accretion events ( $M_{\star} < 10^{7.5} M_{\odot}$ ) that range in dynamical state and are present across wide range of mean Galactocentric distances. Consistent with prior work, our results demonstrate that the inner regions of the stellar halo

should host phase-mixed debris from these objects. In addition, a significant fraction of our low-mass sample are present at high  $\langle R_{\rm GC} \rangle$  values. Moreover, these remain coherent in phase space. While errors in distances and decreasing surface density will impede the detectability of these substructures spatially at large  $R_{\rm GC}$ , these kinematically cold features will be promising to detect in kinematic surveys. Therefore, these simulations suggest that we are not limited to local volumes to find remnants of very early and low-mass accretion events, and point to a great deal of discovery potential for these systems with future astrometric and spectroscopic surveys.

Along those lines, the error bars in Figure 3 (which bracket the 16th–84th range) provide information of the distribution across radii for each disrupted satellite. Given our findings, mergers that deposit the bulk of their stars at the closest Galactocentric distances (namely,  $\langle R_{\rm GC} \rangle \lesssim 30~{\rm kpc} \rangle$ ) have a relatively small, yet noticeable, spread in the Galactocentric distances at which they deposit these stars, ranging from anywhere between a range of 5 to 30 kpc. Conversely, the majority of accretion events that end up depositing the bulk of their stars at large Galactocentric distances (namely, at  $\langle R_{\rm GC} \rangle > 100~{\rm kpc} \rangle$ ) can be divided into two subcategories. The first is comprised by primarily coherent-stream accretions, which have very high spread values (namely, a range greater than  $\sim 30~{\rm kpc}$ ). The second group is populated primarily by

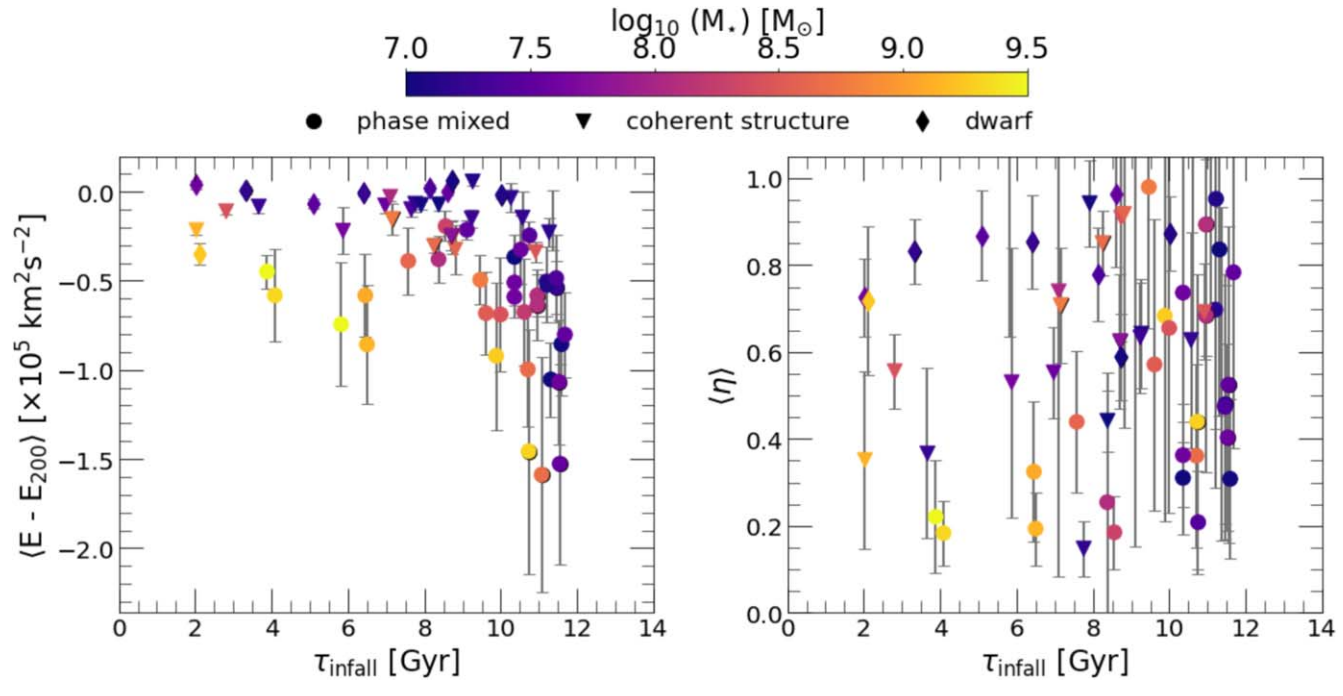


Figure 4. Normalized mean orbital energy (left) and mean orbital circularity (right) for every accretion event (w.r.t. their host Galaxy's potential) at z = 0 as a function of  $\tau_{\text{infall}}$ , color-coded by the respective stellar mass. As in Figure 3, the error bars illustrate the 16th and 84th percentile range.

accretion events classified as present-day dwarf galaxies that present very low ranges, on the order of  $\sim$ 10 kpc.

We note that there are four coherent-stream mergers that present lower spread values, on the order of <15 kpc. We examined the distribution of these disrupted satellites in the X-Y and X-Z projections and found that these mergers present lower spreads in their Galactocentric radii distribution because they present thin and long tidal tails and/or have a significant amount of mass still bound in their progenitor system that has not fully disrupted. This spatial distribution would lead to these debris occupying large Galactocentric distance values, while still maintaining a low spread. Conversely, there is one coherent-stream merger that presents a very large Galactocentric radii distribution, on the order of  $\sim$ 90 kpc. When examining the distribution of star particles belonging to this disrupted satellite in the X-Y and X-Z planes, we found that this accretion event presents a very radial and extended distribution, thus leading to the large Galactocentric radius spread value determined for its given average Galactocentric distance.

In order to contextualize our findings with respect to current/upcoming surveys, we overplot in Figure 3 observing limits estimated from Sanderson et al. (2019) for different stellar tracer populations in the Milky Way. Specifically, we show as red/black lines the assumed limiting magnitude limits for red giant branch (RGB)/main-sequence turn-off (MSTO) stars, two stellar tracer populations that will be advantageous to trace, due to their bright luminosity and populous numbers, respectively (e.g., Cunningham et al. 2019a, 2019b). Dashed lines indicate the distance limit for samples of RGB (shown in red) and MSTO (in black) stars observed by Gaia mission (Gaia Collaboration et al. 2018) and with 4 m class telescope spectroscopy. Dotted lines show estimates of the distance limits for these tracers observed with Rubin Observatory's Legacy Survey of Space Time (LSST; Ivezić et al. 2019). In

Section 6.3, we discuss in detail the implications of our findings in the context of observational work. However, in brief, our results suggest that current astrometric and spectroscopic surveys are only scratching the surface of the debris from cannibalized satellite galaxies that are predicted to inhabit the stellar halo of the Galaxy, and are likely biased to only identifying the most massive and/or the most recently accreted disrupted galaxies. This reasoning is twofold: (1) more massive systems will dominate the local (observable) stellar halo, and thus will likely be more easily detectable based on sheer numbers; and (2) more recently accreted disrupted satellites (e.g., Sagittarius dSph) will still retain easily detectable coherent-stream debris, making them also more easily detectable. The advent of large-scale stellar surveys like LSST, WEAVE, and 4MOST, with its ability to observe stellar tracer populations with high numbers at far larger Galactocentric distances than current surveys, will help make possible such discoveries.

# 4. Orbital Properties

Having studied the resulting spatial distribution of the identified accretion events, in this section we discuss the distribution of their orbital properties. Specifically, we set out to interpret the resulting mean orbital energy, angular momentum, and circularity values (as defined in Table 2) for every merger event as a function of both infall time and stellar mass. As integrals of motion (such as orbital energy and actions) are, under the assumption of a static potential and potential symmetry, invariants, the results obtained in this section will provide insight on how different types of accretion events manifest themselves in key diagnostic orbital planes that can be qualitatively compared to large-scale observations of stars in the MW (for example, see Santistevan et al. (2023)).

#### 4.1. Orbital Energy

We begin by examining the resulting (normalized) mean orbital energy in the left panel of Figure 4 as a function of  $au_{\text{infall}}$ , where each merger event is color-coded by its respective stellar mass. Here, the mean orbital energy (E) is the mean kinetic and potential energy per unit mass over all particles that belong to each accretion event at z = 0 (namely,  $E = \Phi + K$ , where  $\Phi$  and K are the mean potential energy per unit mass and mean kinetic energy per unit mass, respectively), normalized to the mean orbital energy value at  $R = 200 \,\mathrm{kpc}$  (which we denoted as  $E_{200}$ ). This yields the mean normalized orbital energy  $\langle E - E_{200} \rangle$ . Furthermore, the potential  $(\Phi)$ , taken from Arora et al. (2022), is comprised of three components: an NFW profile for the dark matter halo (Navarro et al. 1996), a spherical potential model for the central bulge, and a Miyamoto-Nagai profile modeling the cylindrical disk of the simulation (Miyamoto & Nagai 1975). This potential is then propagated in simulation time as a time-evolving multipole potential, modeled using a low-order multipole expansion assuming axisymmetry, evaluated at each snapshot independently. For the case of the kinetic energy term, we determine this quantity per unit mass as  $K = \frac{1}{2}v^2$ .

Figure 4 shows that mean orbital energy is strongly dependent on the stellar mass and infall time of a disrupted satellite, and it follows a similar relation to that observed in Figure 3. This result is not surprising, given that the potential energy is inversely proportional to galactocentric radius. We find that, at early times ( $\tau_{\rm infall} \gtrsim 11$  Gyr), accretion events have a wide range of orbital energies, spanning from  $-1.75 \times 10^5 < \langle E - E_{200} \rangle < 0.05 \times 10^5 \text{ km}^2 \text{ s}^{-2}$ , whereas at more recent times (namely,  $\tau_{\text{infall}} \lesssim 7$  Gyr), accretion events have a smaller range in mean orbital energies  $(-0.75 \times 10^5 < \langle E - E_{200} \rangle < 0.05 \times 10^5 \text{ km}^2 \text{ s}^{-2})$ . At fixed infall time, higher-mass accretion events deposit the bulk of their stars at lower orbital energies than their lower-mass counterparts, with the minimum orbital energy increasing over time, due to the growth of the MW-like host halo potential. Furthermore, we find that, for fixed  $\tau_{infall}$ , accretion events that deposit the bulk of their stars at lower energies are primarily classified as phase-mixed mergers. Conversely, we find the mergers at the highest orbital energies  $(\langle E - E_{200} \rangle \gtrsim -0.15 \times 10^5 \text{ km}^2 \text{ s}^{-2})$  to be primarily either coherent-stream and/or present-day dwarf galaxies.

The spread in the orbital energy values, defined as the range between the 16th and 84th percentiles, are also shown in the left panel of Figure 4 as error bars. Here, we see that accretion events at earlier  $\tau_{infall}$  have a much wider range in the spread of their orbital energy values. At fixed infall time, we find that more massive accretion events have on average higher spreads in their energies than their lower-mass counterparts. Moreover, we also see that the value of the spread decreases with decreasing  $\tau_{\text{infall}}$ . This is likely due to the combination of two effects: first, the potential of the host changes over time, and these changes are more drastic at early times, causing the orbital energies of the stars of the disrupted satellite to occupy a wider range of values; second, the value of the potential energy at R = 200 kpc increases over time, due to the overall growth of the host halo, and thus the dynamical times are longer. This results in later accreted mergers taking longer to phase mix and having less time to do so. Both the change in the potential of the host, as well as the mass ratio between the host and the disrupted galaxy, are mechanisms that result in debris from

recent accretion events having lower spreads in their orbital energies.

# 4.2. Circularity

We now focus on the mean circularity  $(\langle \eta \rangle)^{14}$  values for star particles associated with all the accretion events studied in this work. As described in Table 2,  $\eta$  is defined as the ratio of the total angular momentum of a merger with the angular momentum of a circular orbit with the same orbital energy. More explicitly, the circularity term was calculated as a weighted sum of the angular momenta (and respective  $L_{\rm circ}$  values) for each star particle in each merger, and can be defined analytically as

$$\langle \eta \rangle = \left\langle \frac{L_{\text{tot}}(E)}{L_{\text{circ}}(E)} \right\rangle,$$
 (2)

where  $L_{tot}(E)$  and E are the angular momentum per unit mass and orbital energy per unit mass, respectively, for every star particle associated with an accretion event, and  $L_{circ}(E)$  is the angular momentum per unit mass of a circular orbit with the same E (namely  $L_{circ}(E) = r_{circ}(E) \times v_{circ}(E)$ ; see Table 2 for further details). Thus,  $\langle \eta \rangle = 1$  corresponds to a perfectly circular orbit at z = 0, while  $\langle \eta \rangle = 0$  corresponds to a perfectly radial orbit. We note that there are two mergers, one in m12b and one in m12m, for which we obtained a circularity value of  $\langle \eta \rangle > 1$  (1.28 and 3.12, respectively), which is physically unreasonable. Panithanpaisal et al. (2021) argue that the timedependent and nonspherically symmetric potential, especially at early times, is the culprit for such problematic circularity values. Thus, we choose to exclude these mergers when examining the resulting circularities of accretion events in the set of MW-like galaxies studied. As we only remove two mergers from our sample, we are confident that the exclusion of these accretion events will not impact any conclusions derived from our results.

The right panel of Figure 4 displays the resulting mean orbital circularity values obtained for each accretion event as a function of  $\tau_{\text{infall}}$ , color-coded by stellar mass. The error bars in this plot show the spread in the orbital energy and circularity values, defined as the 16th–84th percentile ranges for each object. From our results, we find that there is no clear relation between  $\langle \eta \rangle$  with either infall time nor stellar mass, as mergers of different  $\tau_{\text{infall}}$  and  $M_{\star}$  present a wide variety of  $\langle \eta \rangle$  values. Interestingly, we find that, on average, phase-mixed accretion events present lower  $\langle \eta \rangle$  values when compared to those mergers classified as coherent streams and/or dwarfs. This result is in agreement with Johnston et al. (2008) and suggests that surviving satellites are on more circular orbits than their phase-mixed counterparts (see also Santistevan et al. (2023)). However, we do note that there is a spread, and that there are a small number of phase-mixed mergers that present higher circularity values as well as a small number of coherentstream/dwarfs mergers that present circularity values on the order of  $\langle \eta \rangle \sim 0.2$ .

<sup>&</sup>lt;sup>14</sup> These values were computed using the potentials determined in Arora et al. (2022), utilizing the AGAMA Vasiliev (2019) galactic dynamics package.

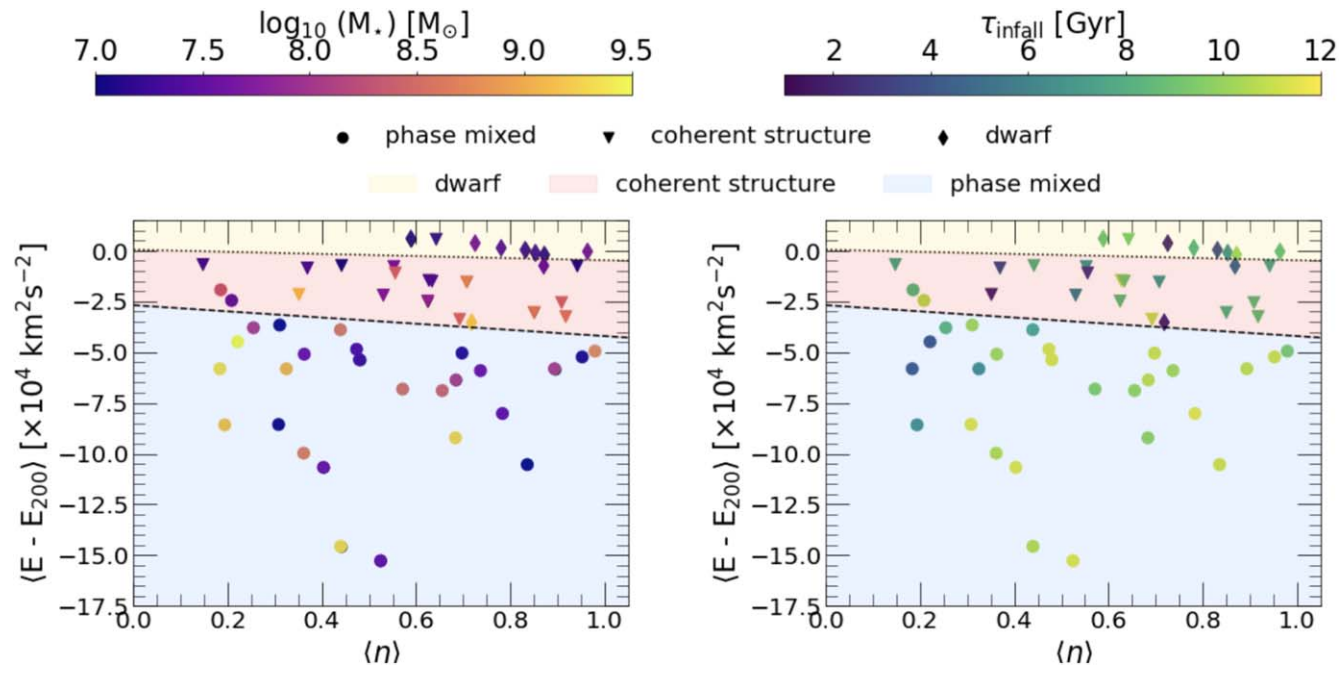


Figure 5. Mean orbital energy as a function of mean circularity for all accretion events studied in this work, color-coded by stellar mass (left) and infall time (right). Indicated in these plots are three groups (shaded regions) corresponding to the predictions determined using the support vector machine classifier sklearn.svm. SVC (see text for details). The slope and intercept values of the two division lines are slope:-1.52(-0.52); intercept:-2.69(0.05) for the dashed(dotted) lines, respectively. It is possible to use the mean orbital energy and circularity values of a disrupted galaxy to statistically predict its present-day dynamical state.

#### 4.3. The Link between Orbital Energy and Circularity

Having examined all the orbital properties of accretion events in MW-like halos independently, we now set out to study the position of such mergers in a combination of orbital parameters. We show the resulting mean orbital energy values for each accretion event as a function of their mean circularity in Figure 5. In addition, we quantify the distinction of different dynamical state classes of accretion events by training a linear kernel Support Vector Machine (SVM) classifier using the sklearn.svm.SVC routine and utilizing as input the orbital energy and circularity values of every merger. Specifically, we set the kernel to be linear and define the regularization parameter to 1. Our training set comprises of all mergers in the m12b, m12c, m12f, m12i, and m12m simulations, and our validation set is comprised of all mergers in the m12r and m12w simulations. We perform this test for two independent samples: first, for phase-mixed and coherent structure mergers; and second, for coherent structure and dwarf disrupted satellites. The results from this SVM classifier yield two linear trends able to distinguish accretion events in Figure 5 based on dynamical state, and are shown as the shaded regions in this diagram.

From our results, it is evident that an accretion event's present-day dynamical state is clearly dependent on its orbital energy and circularity, as the dwarf, coherent-stream, and phase-mixed mergers occupy different loci in this plane. In detail, we find that the dwarf mergers occupy a position at high orbital energies and high circularities, congregating in a narrow locus at the top right corner of the diagram. Conversely, we find that phase-mixed mergers, which present a larger range in mean orbital energies, present a wide range of mean circularity values. However, these types of accretion events all sit at lower orbital energies when compared to their dwarf counterparts. Last, occupying a locus in between the dwarf and phase-mixed

mergers, we find the coherent streams, which present relatively high orbital energies and a wide range of circularities. This projection (or view) of orbital parameters usefully summarizes the dependence of stellar mass and infall time on the resulting mean orbital energy and circularity (and therefore, by definition, also with angular momentum). Of particular importance is the fact that this orbital plane illustrates the wide variety of orbits mergers of similar mass and infall time can adopt, and how dependent these distributions are on the initial conditions of the accretion event.

# 5. Chemical Properties

We next examine the position of the mergers in the  $\alpha$ –Fe plane. As the chemistry of a system should remain constant over time after a satellite is consumed by a larger host, given that its star formation ceases due to gas being stripped (e.g., Robertson et al. 2005; Font et al. 2006), the results from this examination should serve as a strong diagnostic to distinguish different types of accretion events.

The distribution of stars in the  $[\alpha/\text{Fe}]$ –[Fe/H] is an indicator of the chemical evolution and star formation history (SFH) of the population. Understanding the  $[\alpha/\text{Fe}]$  and [Fe/H] abundances of stars associated with a galaxy can help place strong constraints on its formation and evolution. When applied to stars from satellites accreted by an MW-like galaxy, their distribution in this chemical plane is a clear diagnostic of the time at which the accreted satellite ceased star formation (e.g., Robertson et al. 2005; Font et al. 2006; Mackereth et al. 2019; Khoperskov et al. 2022b). It also provides an opportunity to study how lower-mass galaxies chemically evolved in the early universe (e.g., Corlies et al. 2018). For example, Panithanpaisal et al. (2021) and Cunningham et al. (2022) showed how the progenitors of low- to intermediate-mass streams differed chemically from the present-day population of satellite

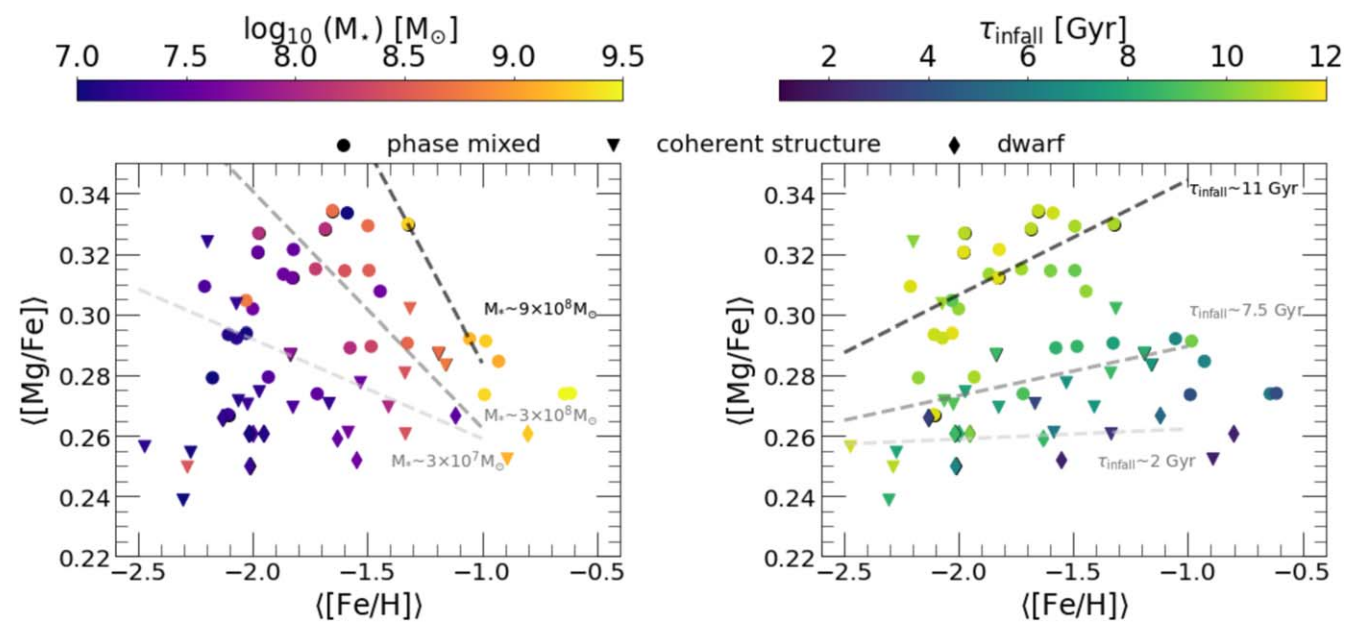


Figure 6. Mean [Mg/Fe] and [Fe/H] values for all the accretion events identified in this work, color-coded by stellar mass (left) and infall time (right). It is evident that these chemical properties are intimately related with the progenitor's stellar mass and infall time. To illustrate this point, we show the isomass (namely for  $M_{\star}=3\times10^7/3\times10^8/9\times10^8~M_{\odot}$ ) and isoage (namely for  $\tau_{\rm infall}=2/7.5/10~{\rm Gyr}$ ) trends in light gray, gray, and black. For example, more massive and/or earlier mergers on average present higher mean [Mg/Fe] values at fixed [Fe/H]. The average spread values, defined as the mean of the 16th and 84th percentiles, are [Mg/Fe]  $\pm$  0.06 and [Fe/H]  $\pm$  0.33 for phase-mixed debris, [Mg/Fe]  $\pm$  0.08 and [Fe/H]  $\pm$  0.39 for coherent structure debris, and [Mg/Fe]  $\pm$  0.08 and [Fe/H]  $\pm$  0.40 for dwarf/satellites.

galaxies. This result emphasizes the ability to use these simulations to gain a deeper understanding of how chemical evolution in low- and intermediate-mass galaxies has varied across cosmic time.

In Figure 6, we show the mean iron metallicity versus the mean magnesium abundance ([Mg/Fe]; we use Mg as our  $\alpha$  element), color-coded by their stellar mass (left) and by their infall time (right). We note that the average spread values, defined as the mean of the difference between the 84th and 16th percentiles, is [Mg/Fe]  $\pm$  0.06 and [Fe/H]  $\pm$  0.33 for phase-mixed debris, [Mg/Fe]  $\pm$  0.08 and [Fe/H]  $\pm$  0.39 for coherent structure debris, and [Mg/Fe]  $\pm$  0.08 and [Fe/H]  $\pm$  0.40 for dwarf/satellites.

Our results show that there is a strong dependence of the position of the bulk of the stars of accretion events in the [Mg/ Fe]-[Fe/H] plane with stellar mass and infall time, which subsequently leads to a relationship with its dynamical state. Focusing on the left panel of Figure 6, we find that more massive accretion events have a higher mean [Fe/H] for fixed mean [Mg/Fe] when compared to their lower-mass counterparts, and that such relation is consistent across all  $\langle [Mg/Fe] \rangle$ values. This effect is due to the mass-[Fe/H] relationship of galaxies (Kirby et al. 2013; Hidalgo 2017), where those satellite galaxies that are more massive will have enriched their ISM with more metals when compared to the lower-mass counterparts. Similarly, at constant ([Fe/H]), we find that lower-mass accretion events present overall lower mean [Mg/ Fe] when compared to their higher stellar mass siblings (see also Samuel et al. (2022)). This difference is due to the lowermass systems overall having lower and/or specific star formation rates, which subsequently leads to less SNII explosions per unit mass and a lower proportional production of  $\alpha$  elements and Fe (see A. C. Mason et al 2022, in preparation). If one now focuses on the right panel of Figure 6, where the mergers are color-coded by their respective  $au_{ ext{infall}}$ 

values, our results reveal another set of trends. Here, we find that, for fixed mean [Fe/H], disrupted satellites that get engulfed by their host MW galaxies at earlier times (i.e., high  $\tau_{\rm infall}$ ) display higher mean [Mg/Fe] values when compared to accretion events that get accreted at later times (i.e., lower  $au_{\rm infall}$ values). Additionally, we find that those accretion events classified as phase-mixed typically present higher  $\langle [Mg/Fe] \rangle$ values for fixed  $\langle [Fe/H] \rangle$  when compared to those mergers classified as coherent streams and/or dwarfs. We reason that this is due to phase-mixed accretion events generally being quenched earlier when compared to coherent structures and/or dwarf satellites. Therefore, for phase-mixed debris to reach a given stellar mass (and therefore a given [Fe/H]), their star formation rate must be higher/more efficient than in lower stellar mass at similar [Fe/H]. Conversely, the latter will have a lower, but more prolonged, star formation history (this was also shown in detail in a recent work by Cunningham et al. (2022) using the same suite of simulations, Figure 3).

We note that the relationship between  $\langle [Mg/Fe] \rangle$ ,  $\langle [Fe/H] \rangle$ , and peak stellar mass for the accretion events identified in this work reveal diagonal isomass trends in this plane, where for fixed stellar mass, an accretion event can be positioned in the [Mg/Fe]–[Fe/H] plane along a diagonal line that decreases in [Fe/H] with increasing [Mg/Fe]. We also note that such isomass trends observed in the left-hand side of Figure 6 are dependent on  $\tau_{infall}$ , where those accretion events of a given stellar mass that are accreted at higher  $\tau_{infall}$  values present a higher mean [Mg/Fe] and lower mean [Fe/H] when compared to mergers of similar mass and smaller  $\tau_{infall}$ .

The intricate relationships found between these key parameters are intimately linked to the star formation history and chemical evolution of the accreted satellite galaxy. Our results have confirmed previous expectations (Robertson et al. 2005; Font et al. 2006; Johnston et al. 2008; Mackereth et al. 2019) that, for fixed mean [Fe/H], more massive and/or earlier

accreted systems present a higher mean [Mg/Fe] value when compared to their lower-mass and/or later accreted siblings. At fixed  $\tau_{\rm infall}$ , this is likely because more massive systems have had a larger number of supernovae (SN) contributions, which pollute the ISM with (primarily)  $\alpha$  elements (for the case of core-collapse SN –SNII–) and Fe (for the case of SN type Ia – SNIa–), due to their higher star formation rate (SFR) when compared to lower-mass systems, which have a slower SFR and smaller number of SN explosions.

Along those lines, for fixed stellar mass, those systems that merged at an earlier lookback time (namely, high  $\tau_{\rm infall}$  values) would have had their star formation quenched earlier. This results in these earlier mergers having a shorter time to evolve chemically, yielding a resulting position in the [Mg/Fe]–[Fe/H] plane of higher mean [Mg/Fe] and lower mean [Fe/H] values when compared to their later accreted and similar-mass counterparts, which would have had more time to evolve chemically and enrich their ISM with heavier metals (like Fe) from delayed SNIa, diluting the [Mg/Fe] ratio while increasing [Fe/H].

The results obtained from examining the mean [Mg/Fe] and [Fe/H] abundances disclose a relationship between an accreted population's chemistry and corresponding stellar mass and infall time. This result is not surprising, given that the chemical evolution of a galaxy will be governed by the amount of time such system is able to evolve before being accreted (and ceasing star formation), and by the amount of gas such system is able to turn into stars (i.e., its star formation), which in turn is intimately linked to the mass of the system. In more detail, the isomass and isoage relations observed for the accretion events studied in Figure 6 are a clear manifestation of the evolution of the mass-metallicity relationship of galaxies across time. To summarize, the clear relationship revealed between the (Mg/ Fe] and ([Fe/H]) abundances, the stellar mass, and the infall time of each accretion event is strong and serves as a powerful tool for disentangling the properties of such mergers.

As the metallicity in the FIRE simulations does not precisely match the observations (Escala et al. 2018; Wheeler et al. 2019), we note that these results should be taken as qualitative. Our findings on the chemical properties of these disrupted satellites should not be used as a quantitative measure in order to predict the stellar mass and infall time of debris identified in the stellar halo of the MW conjectured to originate from cannibalized satellites. Instead, we suggest that the isomass and isoage relations shown in Figure 6 should be used as qualitative blueprints for understanding how different accretion events manifest themselves in a fundamental chemical composition plane, as the general trends and relationships with the chemical properties of these systems are still viable.

Furthermore, because particle initialization in the FIRE-2 models prescribes star particles to be born with a primordial [Fe/H] = -4 and  $[\alpha/Fe] = 0$ , disrupted satellites that present a lower  $\langle [Fe/H] \rangle$  value will on average display a much lower  $\langle [Mg/Fe] \rangle$  than expected (for example, see Font et al. (2006)). This is what causes the decline in the trend of  $\langle [Mg/Fe] \rangle$  below  $\langle [Fe/H] \rangle < -2$  in Figure 6, and it also causes these disrupted satellites to present unphysically low  $\langle [Mg/Fe] \rangle$  values. While this model prescription serves as an added nuisance, we argue that it does not impact the isomass and isoage trends toward higher  $\langle [Fe/H] \rangle$ .

#### 6. Summary and Conclusions

In this paper, we have examined accretion events in a set of seven MW-like halos using the Latte suite of FIRE-2 zoom-in cosmological simulations with the goal of characterizing the relationships between a merger's properties (stellar mass and infall time) and those of the stellar debris it leaves behind. We have explored a range of diagnostic and observable planes, including their spatial distribution (Section 3), orbital properties (Section 4), and chemical properties (Section 5). A summary of the number of disrupted satellites and their properties is listed in Table 1. Our analyses aimed to address three questions: 1) "What are the properties of disrupted satellites?" 2) "Do our expectations of how satellite galaxies get disrupted from tailored/idealized N-body simulations survive in a cosmological context?" 3) "What are the implications for observations?"

## 6.1. What Are the Properties of Disrupted Satellites?

# 6.1.1. Spatial Distribution

- 1. The spatial distribution of stars deposited by disrupted satellites disclose a clear relationship between stellar mass, infall time, and  $\langle R_{\rm GC} \rangle$ , where more massive mergers deposit the bulk of their stars at lower mean Galactocentric distances when compared to lower-mass mergers at fixed  $\tau_{\rm infall}$ . Moreover, we find that the minimum  $\langle R_{\rm GC} \rangle$  value increases with decreasing  $\tau_{\rm infall}$  as the host MW-like halo grows, growing from  $\langle R_{\rm GC} \rangle < 10\,{\rm kpc}$  at  $\tau_{\rm infall} > 10\,{\rm Gyr}$  to  $\langle R_{\rm GC} \rangle > 30\,{\rm kpc}$  at  $\tau_{\rm infall} < 4G\,{\rm yr}$  (for the most massive mergers  $M_{\star} > 10^9\,M_{\odot}$ ).
- 2. Disrupted satellites that deposit the bulk of their stars at higher mean Galactocentric distances (namely,  $\langle R_{\rm GC} \rangle > 40~\rm kpc$ ) present a stellar mass below  $M_{\star} < 10^{7.5} \, M_{\odot}$  and are classified primarily as either coherent-stream/ bound dwarf mergers. This result suggests that there are likely many undiscovered structures/satellites in regions of the Galactic stellar halo beyond  $\sim 30~\rm kpc$ , which should be identifiable with future large-scale stellar surveys (e.g., Gaia, DESI, WEAVE, and 4MOST). This will be particularly exciting for the Rubin/LSST survey, which will be able to detect streams/dwarf galaxies to distances beyond  $R_{\rm GC} > 50~\rm kpc$  (Sanderson et al. 2019).
- 3. Conversely, accretion events that present lower mean Galactocentric distances (namely,  $\langle R_{\rm GC} \rangle < 40 {\rm kpc} \rangle$  are primarily massive (namely,  $M_{\star} > 10^{8.5} M_{\odot}$ ) phase-mixed mergers.

# 6.1.2. Orbital Properties

1. The resulting position occupied by different accretion events in the orbital energy plane studied is strongly dictated by the intimate relationship between a merger's peak stellar mass and infall time. The interplay between these two fundamental parameters governs a disrupted satellite's orbital energy at present day, and it plays a strong role on the dynamical state a merger will adopt at z=0. The left panel of Figure 4 shows that, for fixed  $\tau_{\rm infall}$ , more massive accretion events present overall lower orbital energy values when compared to their lower-mass counterparts. This relation is consistent across all infall times, but the magnitude of the minimum mean orbital energy of a merger increases with

decreasing  $au_{\rm infall}$ , due to the growth of the host MW-like halo over time.

- 2. The dynamical state of a disrupted satellite is also influenced by the system's stellar mass and infall time, because most of the more massive accretion events are typically phase-mixed mergers, whereas lower-mass accretion events are primarily bound coherent streams/ dwarfs.
- 3. Mergers with lower mean orbital energy values (namely, more massive and typically phase-mixed) also display much higher spread in their orbital energy values at lower  $au_{\text{infall}}$  values. This is not observed for the lower-mass coherent-stream/dwarf mergers that are accreted at similar infall times. We speculate that this is due to more massive mergers suffering more from dynamical friction forces than lower-mass accretion events. Dynamical friction is the culprit for the stripping of the orbital energy and angular momentum of these more massive disrupted satellites, forcing them to sink deeper into the host's gravitational potential. This will be further investigated in an upcoming study (T. Donlon et al. 2022, in preparation). Conversely, at  $\tau_{infall} > 10$  Gyr, we see that mergers of all masses display a wide range in the spread values of their orbital energies.
- 4. There is no direct relation between stellar mass and infall time with a disrupted satellite's mean orbital circularity value, which suggests that these two parameters should not play a major role in the radialization of a debris from a cannibalized satellite system. A detailed study of the time evolution of orbital circularity for different mass disrupted satellites is the subject of ongoing work; see T. Donlon et al. (2022, in preparation).
- 5. On average, coherent-stream and bound dwarf accretions present higher mean circularity values ( $\langle \eta \rangle \sim 0.6-1$ ) when compared to their phase-mixed counterparts (that present an average value of  $\langle \eta \rangle \sim 0.2-0.4$ ). However, we do note some exceptions at very high  $\tau_{\rm infall}$ , where some phase-mixed mergers reveal a circularity value close to  $\langle \eta \rangle \sim 0.8$ . Furthermore, at lower  $\tau_{\rm infall}$  we find that coherent streams can present lower circularity values, reaching a value of  $\langle \eta \rangle \sim 0.2$ .

# 6.1.3. Chemical Properties

- 1. The distribution of the accretion events in the [Mg/Fe]– [Fe/H] plane reveals that these chemical properties are clearly correlated with an accretion event's stellar mass and time of accretion, given the isomass and isoage trends observed in the left and right panels of Figure 6, respectively. Here, more massive accretion events (typically classified as phase-mixed) present higher mean [Mg/Fe] for fixed metallicity when compared to their lower-mass mergers, which are typically classified as coherent streams/dwarfs.
- 2. We find that these more massive accretion events that present higher mean [Mg/Fe] values are also accreted earlier when compared to the lower-mass coherent-stream/dwarf mergers that display lower [Mg/Fe] for fixed [Fe/H]. When examining the distribution at fixed [Mg/Fe], we find that the relationship between mass and [Mg/Fe] (at fixed [Fe/H]) evolves with  $\tau_{\rm infall}$ , which we attribute to the evolution of the mass-metallicity relation

of these galaxies across time. Interestingly, our results reveal that, on average, dwarf galaxies have lower mean [Mg/Fe] (across a range in [Fe/H]) when compared to mergers classified as phase-mixed/coherent streams (consistent with the results from Cunningham et al. 2022).

# 6.2. Do Expectations from Prior Simulations Survive in a Highresolution Cosmological Setting?

Overall, our results show that, while the stellar halos of galaxies and the process of hierarchical mass assembly are extremely convoluted, the distribution of the average values of the observable properties of the debris from disrupted satellites follow general expectations from prior simulations when examining them in a high-resolution cosmological setting.

In terms of their spatial and orbital properties, we have found that accretion events that are either more massive or are consumed by the larger host at an earlier time deposit the majority of their stars deeper in the potential well of their host, at lower orbital energies and smaller galactocentric radii values. This result corroborates previous work using *N*-body simulations (e.g., Bullock & Johnston 2005; Johnston et al. 2008; Wetzel 2011; Amorisco 2017a; Jean-Baptiste et al. 2017) and large-volume cosmological simulations with lower resolution (e.g., Cooper et al. 2010; Pillepich et al. 2014; D'Souza & Bell 2018; Pfeffer et al. 2020). It is also in line with recent estimates from cosmological simulations of similar resolution (e.g., Fattahi et al. 2020; Font et al. 2020; Grand et al. 2021; Khoperskov et al. 2022c; Orkney et al. 2022).

Regarding the chemical compositions of disrupted satellites, our findings are also in qualitative agreement with results from *N*-body models (e.g., Font et al. 2006), large-volume cosmological simulations at lower resolution (e.g., Mackereth et al. 2019), and zoom-in simulations of similar resolution (e.g., Khoperskov et al. 2022b).

The advent of the new development of the FIRE-3 simulations (Hopkins et al. 2023), which will provide updated stellar evolution models, chemical evolution yields, microphysics, and updated fitting functions, as well as the advance of other sophisticated cosmological numerical simulations (e.g., ARTEMIS and COLIBRI; Font et al. 2020) will pave the way for a more detailed study of the chemo-dynamical properties of stellar halos in galaxies like our own MW at higher resolution and/or with larger statistical samples. Of particular interest for this topic will be the FIRE-3 simulations, and their ability to implement different nucleosynthetic yields post-processing. This, in combination with exquisite observational data from current/upcoming surveys, will enable a full characterization of the stellar halo of the MW, and it will allow for a full unveiling of the Galaxy's accretion and mass assembly history.

# 6.3. What Do These Results Mean for Future Surveys?

The findings presented in this work have several observable implications for the stellar halo of the Galaxy. The fact that (on average) disrupted satellite galaxies of larger stellar mass deposit the bulk of their stars closer to the center of the MW-like host suggests that the inner regions of the stellar halos of MW-like galaxies are dominated by one to two massive accretions (D'Souza & Bell 2018). This prediction is in line with recent observational discoveries of accreted stellar populations within the inner regions of the Galactic stellar

halo conjectured to be the debris from massive accreted satellites (Belokurov et al. 2018; Helmi et al. 2018; Horta et al. 2021a). However, it is interesting that our results also suggest a significant number of smaller-mass satellites accreted at very early times also must inhabit this region of the MW's stellar halo. Recent observational work has also suggested this is the case for the MW (e.g., Myeong et al. 2019; Koppelman et al. 2020; Naidu et al. 2020). However, the nature of all these recently identified stellar halo populations stills needs to be fully established, as many of the identified halo substructures so far could be the result of one overall ancient massive merger (Amarante et al. 2022; Horta et al. 2022). As we have seen in Figure 3, disrupted satellites can deposit their stars in a wide range of galactocentric radii, which can also appear fragmented in orbital space (Jean-Baptiste et al. 2017; Koppelman et al. 2020; Naidu et al. 2021). The advent of upcoming stellar surveys such as WEAVE, 4MOST, SDSS-V, and later data releases of the Gaia mission will hopefully supply the necessary chemo-dynamical information to fully characterize these stellar populations, which in turn should help settle this matter.

In a similar fashion, our results also suggest that lower-mass disrupted satellites—some of which are also accreted early—should be dominant at at larger galactocentric distances. The debris of such mergers should have also remained coherent in phase space and occupy large galactocentric distances (for example, see Figures 3 and 4), making them detectable in kinematic samples. For the case of these early accreted satellites, this provides a window to study on a star-by-star basis the debris from galaxies formed early in the universe, providing a window to study near-field cosmology. Surveys such as Rubin/LSST, DESI, and (to some extent) Gaia will be extremely helpful for probing these outermost regions of the Galactic stellar halo, and we are hopeful that they will supply the data necessary to study these relics of early galaxy formation.

Finally, we note that the high spread in  $R_{\rm GC}$  values suggests that there is likely a wealth of halo substructure in the Galactic stellar halo that is yet to be characterized and that belongs to accretion events already discovered. Characterizing the properties of these stellar populations and comparing them to theoretical models will lead to a deeper understanding of how satellite galaxies get engulfed by larger-mass systems, helping place constraints on the Galaxy's hierarchical mass assembly.

D.H. thanks Melissa Ness for helpful discussions. He also thanks Sue, Alex, and Debra for their constant support. E.C.C. acknowledges support for this work provided by NASA through the NASA Hubble Fellowship Program grant HST-HF2-51502.001-A awarded by the Space Telescope Science Institute, which is operated by the Association of Universities for Research in Astronomy, Inc., for NASA, under contract NAS5-26555. R.E.S. acknowledges support from NSF grant AST-2007232 and NASA grant 19-ATP19-0068, from the Research Corporation through the Scialog Fellows program on Time Domain Astronomy, and from HST-AR-15809 from the Space Telescope Science Institute (STScI), which is operated by AURA, Inc., under NASA contract NAS5-26555. A.W. received support from: NSF via CAREER award AST-2045928 and grant AST-2107772; NASA ATP grant 80NSSC20K0513; HST grants AR-15809, GO-15902,

GO-16273 from STScI. C.A.F.G. was supported by NSF through grants AST-1715216, AST-2108230, and CAREER award AST-1652522; by NASA through grants 17-ATP17-0067 and 21-ATP21-0036; by STScI through grants HST-AR-16124.001-A and HST-GO-16730.016-A; by CXO through grant TM2-23005X; and by the Research Corporation for Science Advancement through a Cottrell Scholar Award.

The simulations were run using: XSEDE, supported by NSF grant ACI-1548562; Blue Waters, supported by the NSF; Frontera allocations AST21010 and AST20016, supported by the NSF and TACC; and Pleiades, via the NASA HEC program through the NAS Division at Ames Research Center.

#### **ORCID iDs**

```
Danny Horta  https://orcid.org/0000-0003-1856-2151
Emily C. Cunningham  https://orcid.org/0000-0002-6993-0826
Robyn E. Sanderson  https://orcid.org/0000-0003-3939-3297
Kathryn V. Johnston  https://orcid.org/0000-0001-6244-6727
Nondh Panithanpaisal  https://orcid.org/0000-0001-5214-8822
Arpit Arora  https://orcid.org/0000-0002-8354-7356
Lina Necib  https://orcid.org/0000-0003-2806-1414
Andrew Wetzel  https://orcid.org/0000-0003-0603-8942
Jeremy Bailin  https://orcid.org/0000-0001-6380-010X
Claude-André Faucher-Giguère  https://orcid.org/0000-0002-4900-6628
```

# References

```
Allende Prieto, C., Cooper, A. P., Dey, A., et al. 2020, RNAAS, 4, 188
Amarante, J. A. S., Debattista, V. P., Beraldo E Silva, L., Laporte, C. F. P., &
   Deg, N. 2022, ApJ, 937, 12
Amorisco, N. C. 2017a, MNRAS, 464, 2882
Amorisco, N. C. 2017b, MNRAS, 469, L48
Arora, A., Sanderson, R. E., Panithanpaisal, N., et al. 2022, ApJ, 939, 2
Atkinson, A. M., Abraham, R. G., & Ferguson, A. M. N. 2013, ApJ, 765, 28
Behroozi, P. S., Wechsler, R. H., & Wu, H.-Y. 2013a, ApJ, 762, 109
Behroozi, P. S., Wechsler, R. H., Wu, H.-Y., et al. 2013b, ApJ, 763, 18
Bellardini, M. A., Wetzel, A., Loebman, S. R., et al. 2021, MNRAS, 505, 4586
Belokurov, V., Erkal, D., Evans, N. W., Koposov, S. E., & Deason, A. J. 2018,
   MNRAS, 478, 611
Bonaca, A., Conroy, C., Wetzel, A., Hopkins, P. F., & Kereš, D. 2017, ApJ,
  845, 101
Buder, S., Lind, K., Ness, M. K., et al. 2022, MNRAS, 510, 2407
Bullock, J. S., & Johnston, K. V. 2005, ApJ, 635, 931
Chiti, A., Frebel, A., Simon, J. D., et al. 2021, NatAs, 5, 392
Conroy, C., Naidu, R. P., Garavito-Camargo, N., et al. 2021, Natur, 592, 534
Conroy, C., Bonaca, A., Cargile, P., et al. 2019, ApJ, 883, 107
Cooper, A. P., Cole, S., Frenk, C. S., et al. 2010, MNRAS, 406, 744
Corlies, L., Johnston, K. V., & Wise, J. H. 2018, MNRAS, 475, 4868
Crnojević, D., Sand, D. J., Spekkens, K., et al. 2016, ApJ, 823, 19
Cui, X.-Q., Zhao, Y.-H., Chu, Y.-Q., et al. 2012, RAA, 12, 1197
Cunningham, E. C., Deason, A. J., Rockosi, C. M., et al. 2019a, ApJ, 876, 124
Cunningham, E. C., Deason, A. J., Sanderson, R. E., et al. 2019b, ApJ,
   879, 120
Cunningham, E. C., Garavito-Camargo, N., Deason, A. J., et al. 2020, ApJ,
   898, 4
Cunningham, E. C., Sanderson, R. E., Johnston, K. V., et al. 2022, ApJ,
Dalton, G., Trager, S., Abrams, D. C., et al. 2014, Proc. SPIE, 9147, 91470L
de Jong, R. S., Agertz, O., Berbel, A. A., et al. 2019, Msngr, 175, 3
De Lucia, G., & Helmi, A. 2008, MNRAS, 391, 14
De Silva, G. M., Freeman, K. C., Bland-Hawthorn, J., et al. 2015, MNRAS,
Deason, A. J., Belokurov, V., & Evans, N. W. 2011, MNRAS, 416, 2903
```

```
Deason, A. J., Belokurov, V., Evans, N. W., & Johnston, K. V. 2013, ApJ,
Deason, A. J., Belokurov, V., & Sanders, J. L. 2019, MNRAS, 490, 3426
Deason, A. J., Mao, Y.-Y., & Wechsler, R. H. 2016, ApJ, 821, 5
Deason, A. J., Wetzel, A. R., Garrison-Kimmel, S., & Belokurov, V. 2015,
   MNRAS, 453, 3568
Deason, A. J., Erkal, D., Belokurov, V., et al. 2021, MNRAS, 501, 5964
D'Souza, R., & Bell, E. F. 2018, MNRAS, 474, 5300
Duc, P.-A., Cuillandre, J.-C., Karabal, E., et al. 2015, MNRAS, 446, 120
Erkal, D., Deason, A. J., Belokurov, V., et al. 2021, MNRAS, 506, 2677
Escala, I., Wetzel, A., Kirby, E. N., et al. 2018, MNRAS, 474, 2194
Evans, T. A., Fattahi, A., Deason, A. J., & Frenk, C. S. 2020, MNRAS,
   497, 4311
Fattahi, A., Deason, A. J., Frenk, C. S., et al. 2020, MNRAS, 497, 4459
Faucher-Giguère, C.-A., Lidz, A., Zaldarriaga, M., & Hernquist, L. 2009, ApJ,
   703, 1416
Font, A. S., Johnston, K. V., Bullock, J. S., & Robertson, B. E. 2006, ApJ,
  638, 585
Font, A. S., McCarthy, I. G., Crain, R. A., et al. 2011, MNRAS, 416, 2802
Font, A. S., McCarthy, I. G., Poole-Mckenzie, R., et al. 2020, MNRAS,
   498, 1765
Gaia Collaboration, Brown, A. G. A., Vallenari, A., et al. 2018, A&A, 616, A1
Gaia Collaboration, Brown, A. G. A., Vallenari, A., et al. 2021, A&A, 649, A1
Gandhi, P. J., Wetzel, A., Hopkins, P. F., et al. 2022, MNRAS, 516, 1941
Garavito-Camargo, N., Besla, G., Laporte, C. F. P., et al. 2021, ApJ, 919, 109
Garrison-Kimmel, S., Hopkins, P. F., Wetzel, A., et al. 2019a, MNRAS,
   487, 1380
Garrison-Kimmel, S., Wetzel, A., Hopkins, P. F., et al. 2019b, MNRAS,
   489, 4574
Gómez, F. A., Coleman-Smith, C. E., O'Shea, B. W., Tumlinson, J., &
   Wolpert, R. L. 2012, ApJ, 760, 112
Grand, R. J. J., Kawata, D., Belokurov, V., et al. 2020, MNRAS, 497, 1603
Grand, R. J. J., Marinacci, F., Pakmor, R., et al. 2021, MNRAS, 507, 4953
Hahn, O., & Abel, T. 2011, MNRAS, 415, 2101
Hayes, C. R., Majewski, S. R., Shetrone, M., et al. 2018, ApJ, 852, 49
Haywood, M., Di Matteo, P., Lehnert, M. D., et al. 2018, ApJ, 863, 113
Helmi, A., Babusiaux, C., Koppelman, H. H., et al. 2018, Natur, 563, 85
Helmi, A., White, S. D. M., de Zeeuw, P. T., & Zhao, H. 1999, Natur, 402, 53
Hidalgo, S. L. 2017, A&A, 606, A115
Hopkins, P. F. 2015, MNRAS, 450, 53
Hopkins, P. F. 2016, MNRAS, 455, 89
Hopkins, P. F., Wetzel, A., Kereš, D., et al. 2018a, MNRAS, 480, 800
Hopkins, P. F., Wetzel, A., Kereš, D., et al. 2018b, MNRAS, 477, 1578
Hopkins, P. F., Wetzel, A., Wheeler, C., et al. 2023, MNRAS, 519, 3154
Horta, D., Schiavon, R. P., Mackereth, J. T., et al. 2021a, MNRAS, 500, 1385
Horta, D., Mackereth, J. T., Schiavon, R. P., et al. 2021b, MNRAS, 500, 5462
Horta, D., Schiavon, R. P., Mackereth, J. T., et al. 2022, MNRAS, in press
Ibata, R., Martin, N. F., Irwin, M., et al. 2007, ApJ, 671, 1591
Ibata, R. A., Gilmore, G., & Irwin, M. J. 1994, Natur, 370, 194
Iorio, G., & Belokurov, V. 2019, MNRAS, 482, 3868
Iorio, G., Belokurov, V., Erkal, D., et al. 2018, MNRAS, 474, 2142
Ivezić, Ž., Kahn, S. M., Tyson, J. A., et al. 2019, ApJ, 873, 111
Jean-Baptiste, I., Di Matteo, P., Haywood, M., et al. 2017, A&A, 604, A106
Johnston, K. V., Bullock, J. S., Sharma, S., et al. 2008, ApJ, 689, 936
Johnston, K. V., Hernquist, L., & Bolte, M. 1996, ApJ, 465, 278
Khoperskov, S., Minchev, I., Libeskind, N., et al. 2022a, arXiv:2206.04521
Khoperskov, S., Minchev, I., Libeskind, N., et al. 2022b, arXiv:2206.05491
Khoperskov, S., Minchev, I., Libeskind, N., et al. 2022c, arXiv:2206.04522
Kirby, E. N., Cohen, J. G., Guhathakurta, P., et al. 2013, ApJ, 779, 102
Kisku, S., Schiavon, R. P., Horta, D., et al. 2021, MNRAS, 504, 1657
Kollmeier, J. A., Zasowski, G., Rix, H.-W., et al. 2017, arXiv:1711.03234
```

```
Koppelman, H. H., Bos, R. O. Y., & Helmi, A. 2020, A&A, 642, L18
Koppelman, H. H., Helmi, A., Massari, D., Price-Whelan, A. M., &
  Starkenburg, T. K. 2019, A&A, 631, L9
Kroupa, P. 2001, MNRAS, 322, 231
Krumholz, M. R., & Gnedin, N. Y. 2011, ApJ, 729, 36
Leitherer, C., Schaerer, D., Goldader, J. D., et al. 1999, ApJS, 123, 3
Limberg, G., Souza, S. O., Pérez-Villegas, A., et al. 2022, ApJ, 935, 109
Limberg, G., Santucci, R. M., Rossi, S., et al. 2021, ApJL, 913, L28
Ma, X., Hopkins, P. F., Wetzel, A. R., et al. 2017, MNRAS, 467, 2430
Mackereth, J. T., & Bovy, J. 2020, MNRAS, 492, 3631
Mackereth, J. T., Schiavon, R. P., Pfeffer, J., et al. 2019, MNRAS, 482, 3426
Majewski, S. R., Schiavon, R. P., Frinchaboy, P. M., et al. 2017, AJ, 154, 94
Martínez-Delgado, D., Peñarrubia, J., Gabany, R. J., et al. 2008, ApJ, 689, 184
Matsuno, T., Aoki, W., & Suda, T. 2019, ApJL, 874, L35
McCarthy, I. G., Font, A. S., Crain, R. A., et al. 2012, MNRAS, 420, 2245
McConnachie, A. W., Irwin, M. J., Ibata, R. A., et al. 2009, Natur, 461, 66
Miyamoto, M., & Nagai, R. 1975, PASJ, 27, 533
Monachesi, A., Gómez, F. A., Grand, R. J. J., et al. 2019, MNRAS, 485, 2589
Monty, S., Venn, K. A., Lane, J. M. M., Lokhorst, D., & Yong, D. 2020,
  MNRAS, 497, 1236
Myeong, G. C., Vasiliev, E., Iorio, G., Evans, N. W., & Belokurov, V. 2019,
  MNRAS, 488, 1235
Naidu, R. P., Conroy, C., Bonaca, A., et al. 2020, ApJ, 901, 48
Naidu, R. P., Conroy, C., Bonaca, A., et al. 2021, arXiv:2103.03251
Navarro, J. F., Frenk, C. S., & White, S. D. M. 1996, ApJ, 462, 563
Nikakhtar, F., Sanderson, R. E., Wetzel, A., et al. 2021, ApJ, 921, 106
Orkney, M. D. A., Laporte, C. F. P., Grand, R. J. J., et al. 2022, MNRAS Lett.,
  517, L138
Panithanpaisal, N., Sanderson, R. E., Wetzel, A., et al. 2021, ApJ, 920, 10
Pfeffer, J. L., Trujillo-Gomez, S., Kruijssen, J. M. D., et al. 2020, MNRAS,
  499, 4863
Pillepich, A., Vogelsberger, M., Deason, A., et al. 2014, MNRAS, 444, 237
Planck Collaboration, Aghanim, N, Akrami, Y., et al. 2020, A&A, 641, A6
Robertson, B., Bullock, J. S., Font, A. S., Johnston, K. V., & Hernquist, L.
  2005, ApJ, 632, 872
Samuel, J., Wetzel, A., Santistevan, I., et al. 2022, MNRAS, 514, 5276
Samuel, J., Wetzel, A., Tollerud, E., et al. 2020, MNRAS, 491, 1471
Sanderson, R., Carlin, J., Cunningham, E., et al. 2019, BAAS, 51, 347
Sanderson, R. E., Garrison-Kimmel, S., Wetzel, A., et al. 2018, ApJ, 869, 12
Santistevan, I. B., Wetzel, A., El-Badry, K., et al. 2020, MNRAS, 497, 747
Santistevan, I. B., Wetzel, A., Tollerud, E., Sanderson, R. E., & Samuel, J.
  2023, MNRAS, 518, 1427
Schiavon, R. P., Zamora, O., Carrera, R., et al. 2017, MNRAS, 465, 501
Searle, L., & Zinn, R. 1978, ApJ, 225, 357
Shipp, N., Panithanpaisal, N., Necib, L., et al. 2022, arXiv:2208.02255
Steinmetz, M., Guiglion, G., McMillan, P. J., et al. 2020, AJ, 160, 83
Su, K.-Y., Hopkins, P. F., Hayward, C. C., et al. 2017, MNRAS, 471, 144
Tissera, P. B., White, S. D. M., & Scannapieco, C. 2012, MNRAS, 420, 255
Vasiliev, E. 2019, MNRAS, 482, 1525
Vasiliev, E., Belokurov, V., & Erkal, D. 2021, MNRAS, 501, 2279
Veljanoski, J., Mackey, A. D., Ferguson, A. M. N., et al. 2014, MNRAS,
  442, 2929
Wetzel, A., & Garrison-Kimmel, S. 2020a, GizmoAnalysis: Read and Analyze
   Gizmo Simulations, Astrophysics Source Code Library, ascl:2002.015
Wetzel, A., & Garrison-Kimmel, S. 2020b, HaloAnalysis: Read and Analyze
  Halo Catalogs and Merger Trees, Astrophysics Source Code Library,
  ascl:2002.014
Wetzel, A. R. 2011, MNRAS, 412, 49
Wetzel, A. R., Hopkins, P. F., Kim, J.-h., et al. 2016, ApJL, 827, L23
Wheeler, C., Hopkins, P. F., Pace, A. B., et al. 2019, MNRAS, 490, 4447
Yuan, Z., Chang, J., Beers, T. C., & Huang, Y. 2020, ApJL, 898, L37
```